



Enabling Science through European Electron Microscopy

Second report on TEM methods applied to ICT materials

Deliverable D7.2 – V3.2 Final

Delivery date:	M36 December 2021
Lead beneficiary:	GRA, ZAR
Person responsible:	Raul Arenal, Gerald Kothleitner
Deliverable type:	<input checked="" type="checkbox"/> R <input type="checkbox"/> DEM <input type="checkbox"/> DEC <input type="checkbox"/> OTHER <input type="checkbox"/> ETHICS <input type="checkbox"/> ORDP
Dissemination level:	<input checked="" type="checkbox"/> PU <input type="checkbox"/> CO <input type="checkbox"/> EU-RES <input type="checkbox"/> EU-CON <input type="checkbox"/> EU-SEC



THIS PROJECT HAS RECEIVED FUNDING FROM THE EUROPEAN UNION'S HORIZON 2020 RESEARCH AND INNOVATION PROGRAMME UNDER GRANT AGREEMENT NO **823717**

Grant Agreement No:	823802
Funding Instrument:	Research and Innovation Actions (RIA)
Funded under:	H2020-INFRAIA-2018-1: Integrating Activities for Advanced Communities
Starting date:	01.01.2019
Duration:	54 months

Table of contents

Introduction

Task 7.1: Semiconducting and magnetic materials

Task 7.2: Functional complex oxides, carbon and related nanostructures

Task 7.3: Photonic materials

Task 7.4: Sample preparation

Summary

References

Revision history log

Version number	Date of release	Author	Summary of changes
V1		Raul Arenal Cesar Magen Gerald Kothleitner Alexandre Gloter Lunjing Zen Eva Olsson	Preparation of the initial version of the report.
V2		Raul Arenal	Update of the references, text and figures.
V3.0 Final		Raul Arenal	Finalization
V3.1 Final	15.12.2021	Peter van Aken	Minor amendments and approval
V3.2 Final	15.12.2021	Aude Garsès	General review

Introduction

The functionality and availability of future generations of Information and Communications Technologies (ICT) critically depend on the discovery, exploration and understanding of the fundamental physico-chemical principles that underlie the various electronic / magnetic / photonic / semiconducting materials used in the ICT industry. The large diversity of required functionalities and the broad range of materials needed, require powerful characterization techniques, ranging from specimen preparation to diffraction and imaging, electron tomography, spectroscopy, holography and in-situ investigations, with adequate energy and spatial resolution. The work package explores the applicability of TEM in the context of the pertinent physical phenomena and its best use with respect to a certain class of materials. Formally the work is split into four tasks, however, intrinsic to the nature of the materials, some of the results presented within a task, occasionally overlap with others. This deliverable shall emphasize some of the key findings within the 18 to 36 months of the project, and highlights the strengths of (the combination of) techniques used so far.

Task 7.1: Semiconducting and magnetic materials (GRA, ZAR, CHA, TOU*, CAT*)

The relationship between the microstructure and the physical properties of an alloy is of utmost interest - the latter can change dramatically when manipulating the former. Spinodal decomposition of an alloy denotes one way of such a manipulation. In the example shown, a CuFeNi alloy decomposes upon heat treatment into a Cu-rich and a Ni-rich phase, accompanied with a switch from paramagnetic to ferromagnetic behaviour. The left image in Figure 1 reveals the elemental distribution of the elements Fe, Ni and Cu based on the corresponding EDX signals, and displays the segregation into two phases growing along the $[100]$ crystallographic directions. The right image in the panel provides the result of a DPC analysis of a similar region, given as a "colour-wheel" representation. There, the direction of the magnetic induction vectors is plotted as a function of hue, and the colour-wheel inset (in the upper right of the image) reveals the relation of colour and direction. Within the DPC image the micromagnetic structure is discerned and the direction of the magnetization vector (drawn as white arrows) is given for several domains and shows a pattern with 90° and 180° domains, which can be assigned to the $[111]$ orientation of the crystal (publication in preparation).

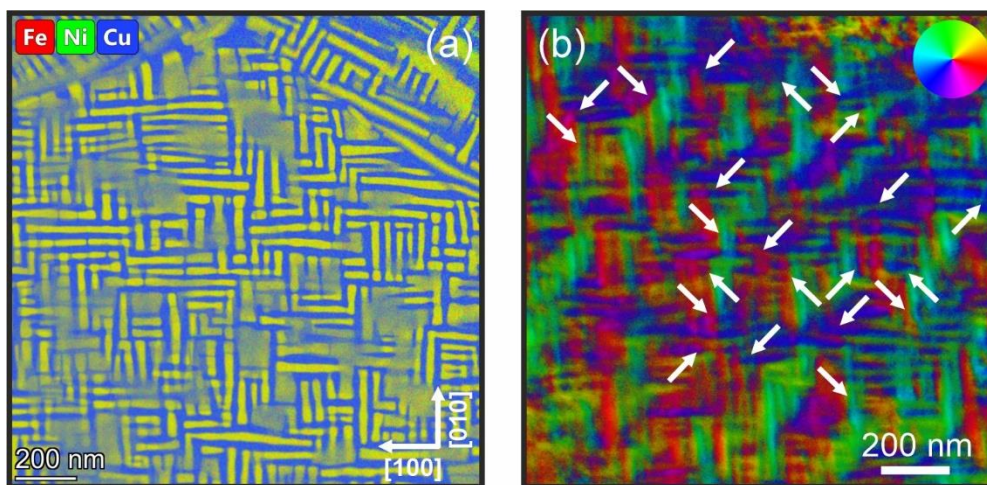


Figure 1: (a) Elemental distribution of Fe, Ni and Cu, extracted from the corresponding EDX signal. Phase segregation along the $[100]$ crystallographic orientation is clearly visible. (b) DPC magnetic induction map containing the micromagnetic domain structure

Semiconducting nanostructures are also key for the development of future ICT technologies. Particularly interesting are semiconductor nanowires, where the 3D architecture and confinement effects produce exciting phenomena with applications in high-speed electronics, sensitive detectors for optical communication, high efficiency solar cells, or quantum computing, among others.

A paradigmatic example is GaAs, which present outstanding charge carrier mobility, and the ability to detect and emit light, with a remarkable performance enhancement in the form of nanostructures such as nanowires. A way to optimize and tune their functional properties is to utilize the coupling between different physical degrees of freedom, such as mechanical strain, electronic structure and electronic properties. A detailed, quantitative and correlative analysis of the coupling of those physical properties in the nanostructures is key to probe the influence of a local deformation in the optoelectronic properties of these nanoscale materials. In this case, a dedicated Hysitron PI95 nanoindentation TEM holder, equipped with an electrical push-to-pull (EPTP) device, was used to apply local stress on single GaAs nanowires, while measuring the local strain by TEM and determining the electrical properties by obtaining simultaneously I-V curves. The in-situ nanometer-scale study of the strain induced by external tensile stress on single GaAs nanowires has been performed by STEM nanobeam electron diffraction (STEM - NBED). Figure 2 displays how the application of stress induces a complex spatial inhomogeneity at all stress levels. The study also shows that the conductivity of the nanowires varied with applied uniaxial tensile stress, showing an initial decrease of $\sim 5\text{--}20\%$ up to a stress of $1\text{--}2$ GPa, subsequently increasing up to the elastic limit of the nanowires. This is attributed to a hole mobility variation due to changes in the valence band structure caused by stress and strain. Meanwhile, monochromated low loss EELS spectroscopy allowed to determine a significant red shift of the band gap caused by the induced strain [1].

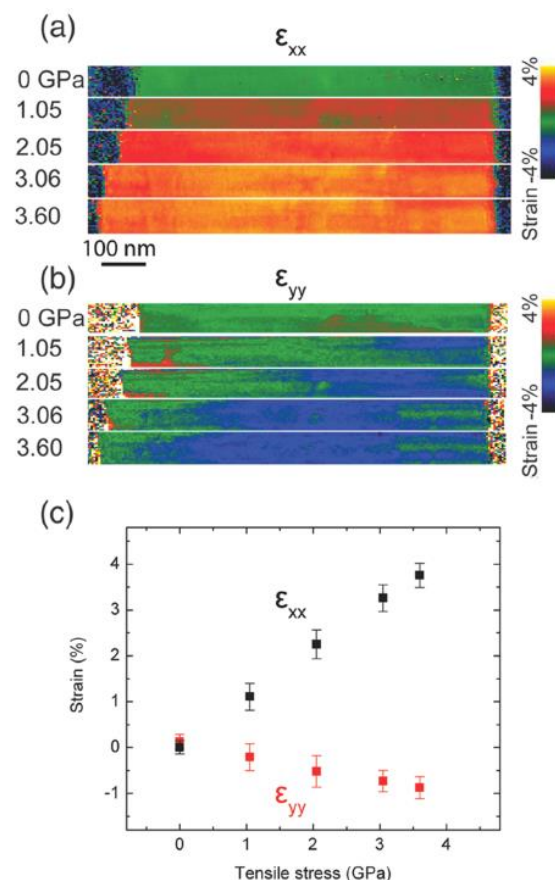


Figure 2: In situ strain mapping by STEM-NBED. (a) Strain maps of the GaAs nanowire under tensile stress, with strain measured along the nanowire length (x) direction. From top to bottom, the tensile stresses applied on the nanowire are 0,

1.05, 2.05, 3.06, and 3.60 GPa, respectively. (b) Strain maps of the GaAs nanowire under tensile stress, with strain measured perpendicular to the nanowire length (y) direction. From top to bottom, the tensile stresses applied on the nanowire are 0, 1.05, 2.05, 3.06, and 3.60 GPa, respectively. (c) Strain distribution within the nanowire as a function of applied tensile stress. Data points are the mean strain values in the strain maps, and error bars correspond to the standard deviation of strain values in the strain maps. The Poisson's ratio of the nanowire is ~ 0.22 along the $[111]$ (~ 0.19 for bulk GaAs). The Young's modulus of the nanowire is ~ 105 GPa (~ 142 GPa for bulk GaAs). [1]

Nanoscale semiconductor–superconductor hybrids are another type of semiconductor heterostructure of great technological interest for ICT, particularly for future quantum computing technologies to store qubits. Such hybrid structures are also responsible for exotic physical phenomena such as topological superconductivity, Majorana Fermions and spin-Cooper pair coupling.

One of the greatest challenges in this field is finding optimal material combinations and growth conditions for heterostructural formation between these materials with the desired properties, for which advanced electron microscopy is indispensable to characterize these novel architectures. In this particular case, HAADF-STEM imaging has been applied to probe the epitaxy and crystal relationship of atomically flat epitaxial Pb thin films grown on the surface of InAs nanowires (Figure 3). The wurtzite InAs nanowires were grown along the $[0001]$ direction by molecular beam epitaxy (MBE), then Pb was grown at 120 K by electron beam evaporation. STEM investigations of the entire nanowire length were performed to analyze how the system accommodates epitaxial strain. No edge dislocations were found in the Pb layer, which indicates that the small strain needed to obtain the epitaxial growth is absorbed. Figure 3e presents an atomic resolution HAADF-STEM micrograph of the cross-sectioned InAs/Pb nanowire shown in Figure 3a. The two grains (Pb-I and Pb-II) form single crystals along their entire nanowire facet, and are merged by a wedge-shaped single-crystalline domain. The inset in Figure 3e shows how the wedge-shaped grain accommodates two coherent grain boundaries and thus reduces the grain boundary energy between the single Pb-I and Pb-II crystals. The strain in InAs and Pb along the transverse direction is observed by comparing the STEM micrograph and the predicted strain-relaxed heteroepitaxial match (Fig. 3f). By utilizing the average InAs $\{1-100\}$ plane spacing as a scale to measure the relative stress in the structure, Pb along the $\langle 11-2 \rangle$ direction was measured to be compressively strained by $\sim 1.7\%$, whereas InAs along the $\langle 11-20 \rangle$ direction was found to be tensile strained by $\sim 0.7\%$. Assuming that the InAs $\{1-100\}$ planes were not heavily influenced by the interface, the compressed Pb and expanded InAs indicate that the transverse bicrystal interfacial match seeks a domain of two interface planes of InAs for three planes of Pb. This single-crystal nature and epitaxial relation between InAs and Pb were observed for all Pb thicknesses analyzed (5–60 nm), confirming the robustness of the method. Furthermore, these highly ordered heterostructures have a critical temperature of 7 K and a superconducting gap of 1.25 meV, which remains hard at 8.5 T, benefiting from the excellent structural quality of the hybrid interface. Additionally, InAs/Pb island devices fabricated using the hybrid nanowires exhibit magnetic field-driven transitions from a Cooper pair to single-electron charging, a prerequisite for use in topological quantum computation [2].

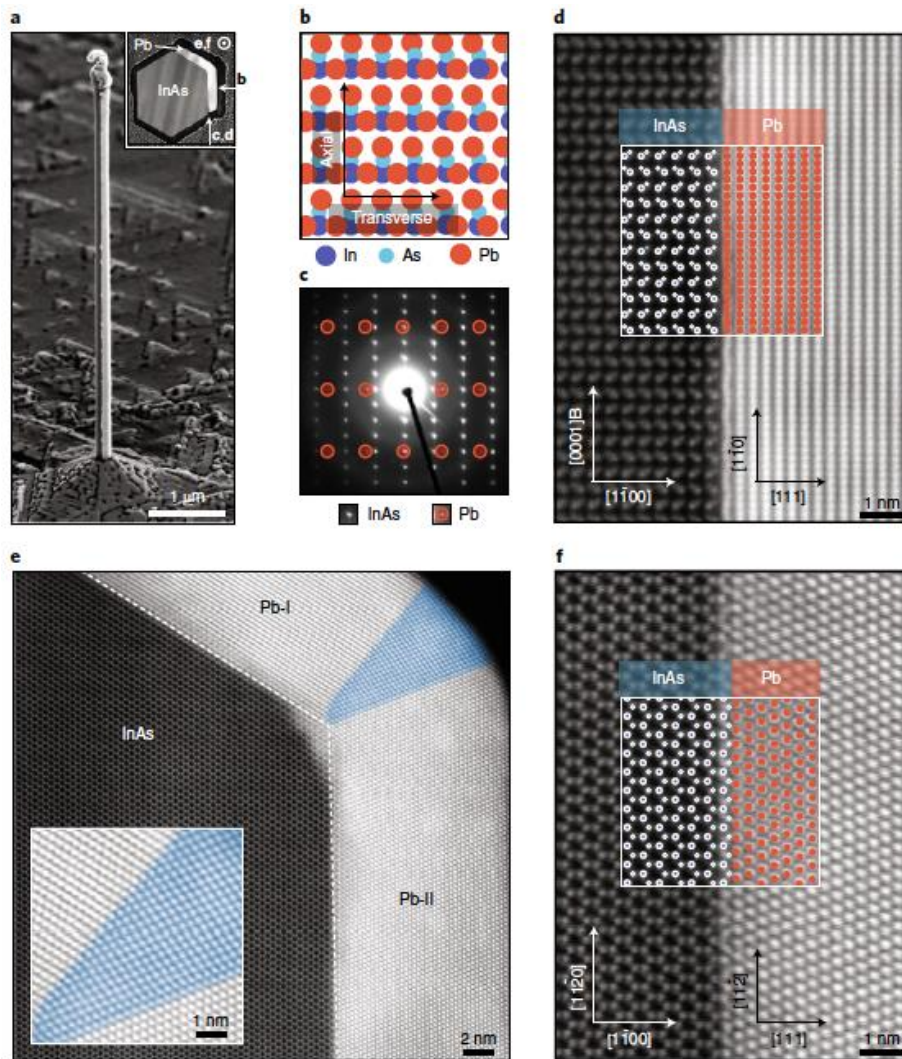


Figure 3: InAs/Pb bicrystal interfacial match. (a) SEM micrograph of an InAs nanowire with a 10 nm Pb thin film on two facets. Inset: HAADF-STEM micrograph of a cross-sectioned InAs/Pb/Si heterostructure. (b) Simulated relaxed bicrystal match between InAs (blue) and Pb (red) viewed normal to the nanowire facet. (c) Selected area electron diffraction pattern of an entire nanowire along the $[11-20]/[11-2]$ direction. Pb diffraction peaks are marked with red semitransparent circles. (d) Atomic resolution HAADF-STEM micrograph of the InAs/Pb interface along the axial $[11-20]/[11-2]$ direction parallel to the nanowire facet. A simulation of the relaxed bicrystal interfacial match is overlaid and marked with a white box. (e) HAADF-STEM micrograph along the $[0001]/[1-10]$ direction of the corner between two adjacent facets, highlighted with white dotted lines. Two single Pb crystals are connected by a wedge-shaped single crystal (false colour blue). Inset: enlarged view. (f) Atomic resolution HAADF-STEM micrograph of the InAs/Pb interface viewed along the transverse direction, as in (e). A theoretical relaxed bulk bicrystal interfacial structure is superimposed on the interface [2].

In the last decade, Focused Electron Beam Induced Deposition (FEBID) has become the ultimate additive nanofabrication technique for the growth of single 3D nanostructures, based on the local decomposition of an organometallic precursor by a finely focused electron beam in the proximity of a substrate, to produce a deposit. This particularly important in the field of nanomagnetism, where 3D nanostructures could be a viable solution to produce future high-density, low-power, fast nanoelectronic devices based on the domain wall conduit in 3D nanomagnets. For this reason, a remarkable effort has been made during the last years to understand and control the physical processes involved in 3D FEBID growth, and their impact on the physico-chemical properties of the nanomagnets, particularly magnetic properties. The ultimate challenge is to implement methods to design 3D magnetic nanostructures with the desired geometry while keeping a high metallic content

and, thus strong magnetism. In this particular case, different electron beam currents and precursor fluxes have been explored to determine their impact on the diameter and content of FEBID nanodeposits based on the standard precursor $\text{Co}_2(\text{CO}_8)_2$. For a given electron beam current, a remarkable dependence of the diameter with the precursor flux (parameterized by the working pressure at the chamber during growth) has been observed, being able to tune the growth geometry from a linear growth (producing ultra-narrow nanowires with high growth rates at high precursor fluxes) to a radial growth (producing thicker nanowires with lower growth rate), as illustrated in Figure 4. Indeed, this change of growth mode perturbs the magnetic configuration in its surroundings (Fig. 4c), and could be exploited to produce modulated structures or bottlenecks that could serve as pinning center for domain walls in future memory and logic devices [15].

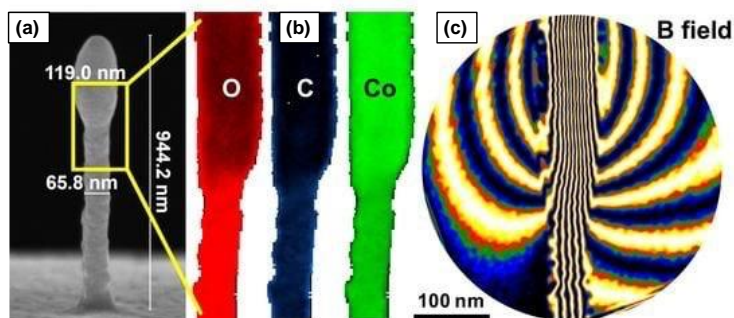


Figure 4: (a) SEM of a 3D FEBID Co nanowire evidencing a transition between the linear regime to the radial regime. (b) STEM-EELS chemical mapping of this crossover region between both regimes analyzed by STEM-EELS. (c) Stray magnetic fields produce at the crossover imaged by off-axis electron holography. [15]

Unfortunately, the extreme control of the diameter is not independent of the cobalt content, and radial-regime grown 3D nanowires present a much higher cobalt content than narrow linear-regime grown nanostructures. Therefore, alternative approaches have been pursued for the growth of ultra-narrow high purity 3D magnetic nanostructures. A very successful one has been the high vacuum thermal annealing to produce a decomposition and volatilization of the organic residues. Ex-situ temperature annealing up to 600°C have been analyzed by HRTEM, STEM-EELS analysis and off-axis electron holography to determine its impact on the functional properties of the 3D FEBID Co nanostructures, with impressive results (Figure 5). While high temperature thermal annealing in vacuum (with no additional reactive gases than the residual ones from ambient atmosphere) transform as-grown 3D Co nanowires are nanocrystalline in nature and of limited (<75 at. %) metallic content into fully crystalline, virtually pure nano-objects with bulk magnetization with no substantial change in geometry or volume. This successful treatment opens the possibility of decoupling the geometry and chemical composition of 3D nanowires in order to produce any desired geometrical design, which can be later purified by ex-situ annealing [15].

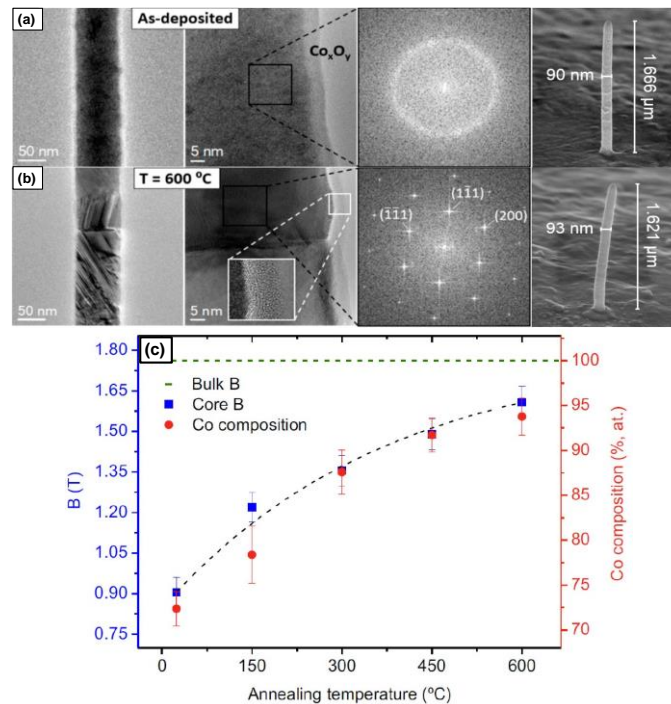


Figure 5: (a) Structural characterization of (a) as-grown and (b) 600°C annealed 3D FEBID Co nanowire characterized by HRTEM. (c) Dependence of the magnetic induction and Co content of the nanowires as a function of the annealing temperature determined by STEM-EELS quantitative analysis and off-axis electron holography. The last column shows SEM images of the nanowires before and after the annealing, evidencing the conservation of the dimensions of the nano-object upon annealing. [15]

Task 7.2: Functional complex oxides, carbon and related nanostructures (ZAR, STU, ORS, TOU*)

Ion conducting materials are critical components of numerous technologies, such as memristive devices, batteries or fuel cells. A method to optimize their ionic conductivity properties is based on tuning the charge carrier concentration by heterovalent doping. Generally dopants are homogeneously distributed, what is called 0D doping, but localized doping (for instance, introducing atomic-thick films of heterovalent cations has been rarely explored and could give rise to new fundamental phenomena and applications on ionic conductors and protonic devices. The possibility of a 2D doping ion conductor has been realized for the first time by inserting unit-cell layers of BaYO_x in thin films of the prototypical proton conductor BaZrO_3 grown by pulsed layer deposition. Aberration corrected STEM has been used to characterize the crystalline quality and chemical distribution of the heterovalent dopants across the layers interfaces. Figure 6 evidences that the interface between the substrate and deposited layers is coherent, and no misfit dislocations are detected along the interface. The resulting superlattice exhibits a high structural quality and displays the nominal superlattice. Both HAADF and ABF images evidence a faint contrast variation at the position of the BaYO_x films, so to characterized the extension of the Y doping across the interfaces, atomically resolved EELS chemical mapping has been performed. Figure 6(c) shows that the Y cations are not located in a single atomic plane, but spread over three unit cells. Laterally averaged Ba, Zr, and Y profiles confirm the nominal superlattice periodicity, where the nominal BaYO_x layer is separated by 6 unit cells of BaZrO_3 regardless of elemental intermixing. The extracted A-to-B-site ratio are 1.05 ± 0.03 . [3]

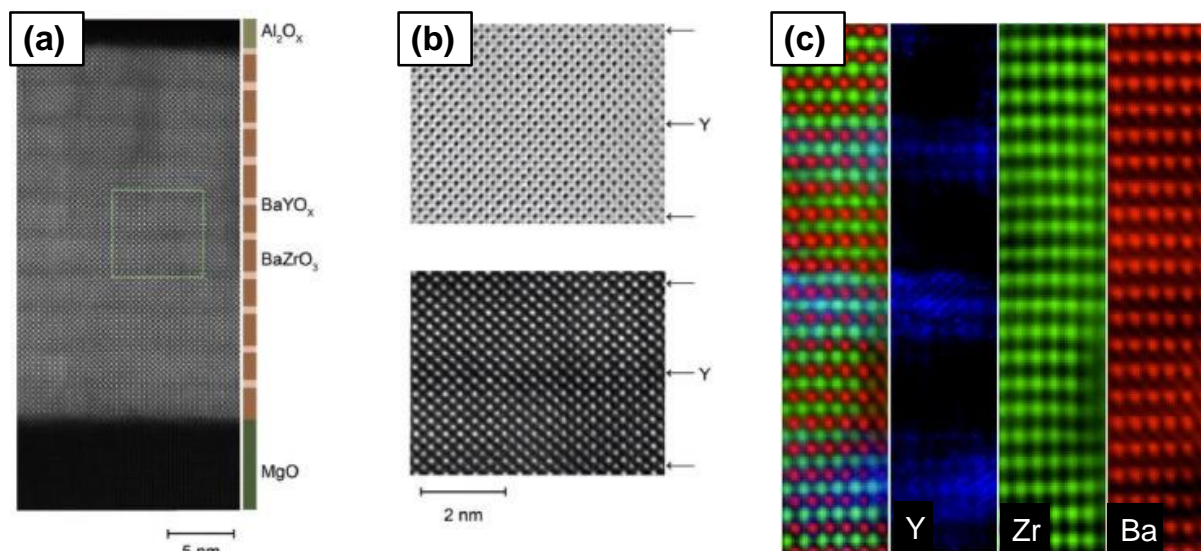


Figure 6: (a) HAADF-STEM High-resolution scanning transmission electron microscopy (HRSTEM) image of a representative $[(\text{BaZrO}_3)_6-(\text{BaYOx})_1]_{10}$ superlattice ($n = 20$, counting the top and bottom interfaces) grown on MgO substrates, c-substrate. (b) Magnified (bottom) annular dark-field and (top) annular bright-field (ABF) images showing the superlattice film with a good structural order. Single YO_x layers are present between BaO layers. Arrows indicate the locations of the single Y atomic layers. (c) Atomic column resolved Ba-M edge (red), Zr-L edge (green), and Y-L edge (blue) elemental maps obtained by fitting the EELS data to the reference spectra using a multiple linear least-squares fitting procedure, and the red-green-blue map of Ba, Zr, and Y. [3]

Another issue regarding ionic conductors is the complexity of their characterization. There are not many analytical tools to monitor and analyze ionic conduction with high spatial resolution and in real time. In principle, inelastic electron tunneling spectroscopy (IETS) offers these capabilities. However, as its spectral resolution is limited by thermal softening of the Fermi–Dirac distribution, tunneling spectroscopy is usually constrained to cryogenic temperatures. This constraint would seem to render tunneling spectroscopy useless for studying ions in motion. Here, the first inelastic tunneling spectroscopy studies above room temperature are reported, Figure 7. For this purpose, dedicated high-temperature-stable tunnel junctions have been used for incorporating an ultrathin tunnel barrier of $\text{BaZrO}_3\text{-BaYO}_x\text{-BaZrO}_3$ acting as well as an efficient proton conduction are developed. The quality of the proton-conducting tunneling barrier as well as its interphase with the bottom electrode of SrRuO_3 are key for optimal tunnel conduction, and have been characterized by HAADF-STEM and atomically resolved EELS mapping. Epitaxial growth has been maintained through the entire stack, and the thicknesses of the individual layers match the intended device structure. The darkish band in the upper part of the SrRuO_3 layer is attributed to local strain generated by misfit dislocations generated at the interface, as electron energy-loss spectroscopy (EELS) O-K edge intensity distribution maps did not show a dip of the oxygen concentration. Subsequent analysis of the vibrational modes of O-H bonds in the BaZrO_3 -based heterostructures of such quality has enabled the detection of protons with a spectral resolution of 20 meV at 400 K (full-width-at-half maximum) is demonstrated, beating the existing prediction for the spectral resolution limit of 186 meV ($5.4 k_B T$) at 400 K. With these advances, inelastic tunneling spectroscopy constitutes a novel, valuable analytical tool for solid-state ionics [4].

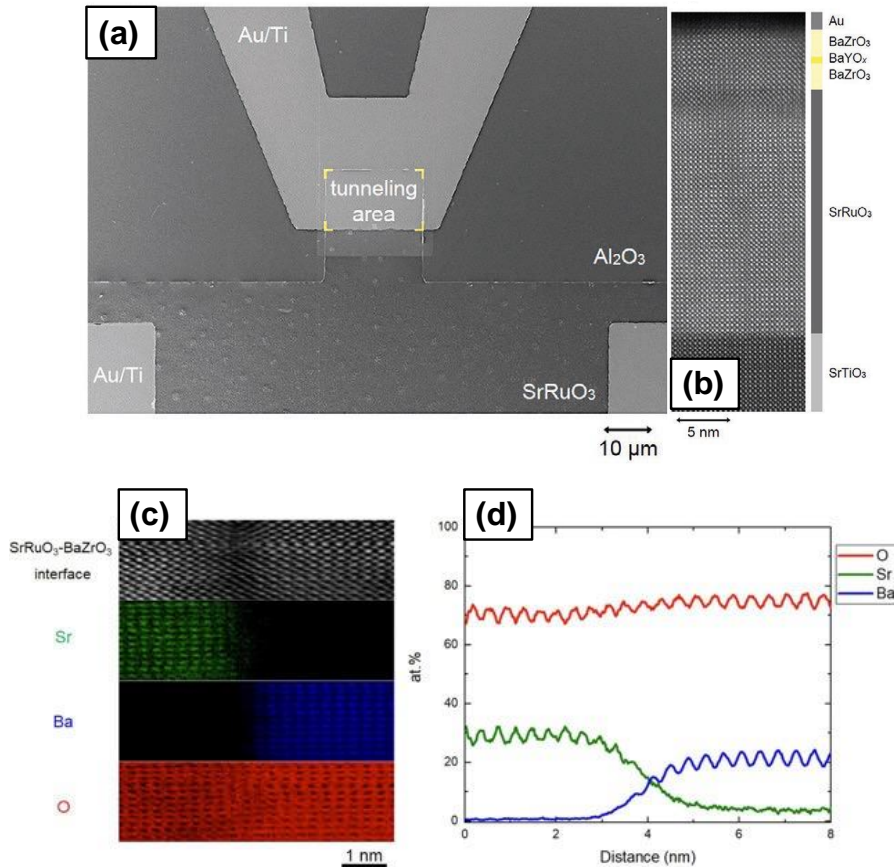


Figure 7: (a) Top view scanning electron microscopy image of a typical tunnel junction. The device shown has a proton-conducting BaZrO₃-BaYO_x-BaZrO₃ barrier with an area of 20 × 20 μm². The yellow marks indicate the corners of the tunnel area. (b) HAADF STEM image showing a cross-sectional cut through a SrTiO₃-SrRuO₃-BaZrO₃-BaYO_x-BaZrO₃-Au tunnel junction. Epitaxial growth has been maintained through the entire stack, and the thicknesses of the individual layers match the intended device structure. The darkish band in the upper part of the SrRuO₃ layer is attributed to local strain generated by misfit dislocations generated at the interface, as electron energy loss spectroscopy (EELS) O-K edge intensity distribution maps did not show a dip of the oxygen concentration [4].

One of the most promising strategies for the development of a new generation of multifunctional low power nanoelectronics is the use of multiferroic oxide thin films. The combination and coupling of different ferroic orders (for instance, magnetic and ferroelectric) turns into an opportunity for an efficient control of the magnetic state by means of electric fields (or vice versa by controlling their polarization state by an external magnetic field). Magneto-electric coupling can be achieved by integrating magnetic and ferroelectric materials into a single heterostructure, or synthesizing single phase multiferroic materials. Bulk multiferroics are scarce though, and approaches such as strain engineering and chemical doping have been explored in the last years to custom tailor multiferroic materials at the nanoscale. In this sense, the predictions that SrMnO₃ could present simultaneous ferroelectric-ferromagnetic states under sufficiently high epitaxial strain or under sufficiently large chemical pressure (i.e., by doping with other alkaline-earth cations like Ba) paved the way to an intensive experimental search. As ferroelectricity in these compounds would be driven by the off-centering of the Mn⁴⁺ magnetic cation, strong magnetoelectric coupling was anticipated. However, strain engineering of thin films presents certain limits, as increasing thickness triggers different relaxation processes, including the presence of strain induced oxygen vacancies, that can severely affect the stabilization of the (multi)ferroic phases.

To explore the impact of relaxation phenomena in this intriguing multiferroic material, we have carried out a thorough investigation of the strain relaxation mechanisms in SrMnO₃ films grown on several

substrates imposing varying degrees of tensile strain from nearly 0% to $\approx 3.8\%$. First, we determine the strain-dependency of the critical thickness (t_c) below which pseudomorphic growth is obtained. Second, the mechanisms of stress relaxation are elucidated, revealing that misfit dislocations and stacking faults accommodate the strain above t_c . Yet, even for films thicker than t_c , the atomic monolayers below t_c are proved to remain fully coherent. Therefore, multiferroicity may also emerge even in films that appear to be partially relaxed. Last, we demonstrate that fully-coherent films with the same thickness present lower oxygen content for increasing tensile mismatch with the substrate. This behavior proves the coupling between the formation of oxygen vacancies and epitaxial strain, in agreement with first-principles calculations, enabling the strain-control of the $\text{Mn}^{3+}/\text{Mn}^{4+}$ ratio, which strongly affect the magnetic and electrical properties. However, the presence of oxygen vacancies/ Mn^{3+} cations reduce the effective epitaxial strain in the SrMnO_3 films and, thus, the accessibility to the strain-induced multiferroic phase. Aberration corrected HAADF-STEM imaging and geometrical phase analysis (GPA) have been used to explore the critical thickness before relaxation and the relaxation mechanisms of SrMnO_3 . For instance, SrMnO_3 can grow uniformly strained on SrTiO_3 substrates up to ~ 15 nm thickness (Figure 8a), even though fine structure spectroscopic analysis of the Mn valence evidences that such epitaxial strain growth of the perovskite phase is only possible by the formation of a substantial oxygen vacancies, with nominal Mn valence as low $+3.6$. For thicker films, oxygen vacancies are not enough and misfit dislocations and stacking faults are formed to relax the elastic stress induced by epitaxial growth, see Figure 8b) [5].

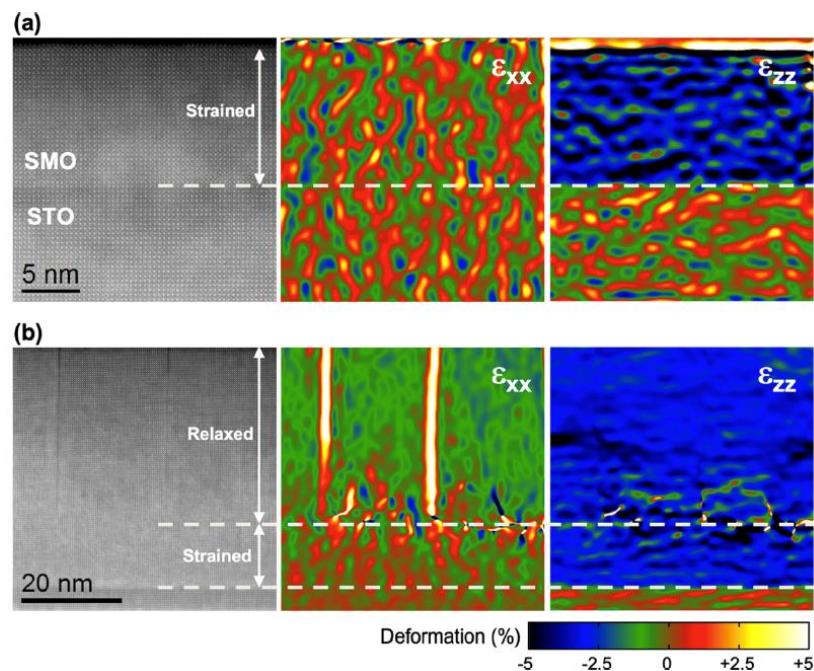


Figure 8: STEM images (left panel) and GPA deformation maps (central panel: in-plane and right panel: out-of-plane) obtained in cross sections of epitaxial SMO films grown on STO, with thicknesses (a) 13 nm (below t_c) and (b) 50 nm (above t_c). [5]

High-resolution STEM-EELS provides information on changes in the composition of crystalline materials at the atomic scale, though a reliable quantitative chemical analysis is often hampered by zone axis conditions, where neighbouring atomic column intensities contribute to the signal at the probe position. On the example of $\text{Ba}_{1.1}\text{La}_{1.9}\text{Fe}_2\text{O}_7$, a second order Ruddlesden-Popper phase, we developed a procedure to determine the concentration of two elements - in our case, barium and lanthanum within the A- sites - within equivalent atomic columns from EELS elemental maps. We took advantage of the large changes in the elemental distribution from column to column and introduced a technique, which substitutes inelastic scattering cross sections during the quantification step and instead uses parameters obtained from the actual experiment. The column intensities were determined by radial integration over each atomic column within each cell of a Voronoi net defined by the local intensity

maxima of the individual columns. The results of the integration are shown in Figure 9. We considered channelling / de-channelling effects via inelastic multi-slice simulations and were thereby able to count occupancies in each atomic column. The EELS quantification results were then used as prior information during the Rietveld refinement in XRD measurements in order to differentiate between barium and lanthanum [6].

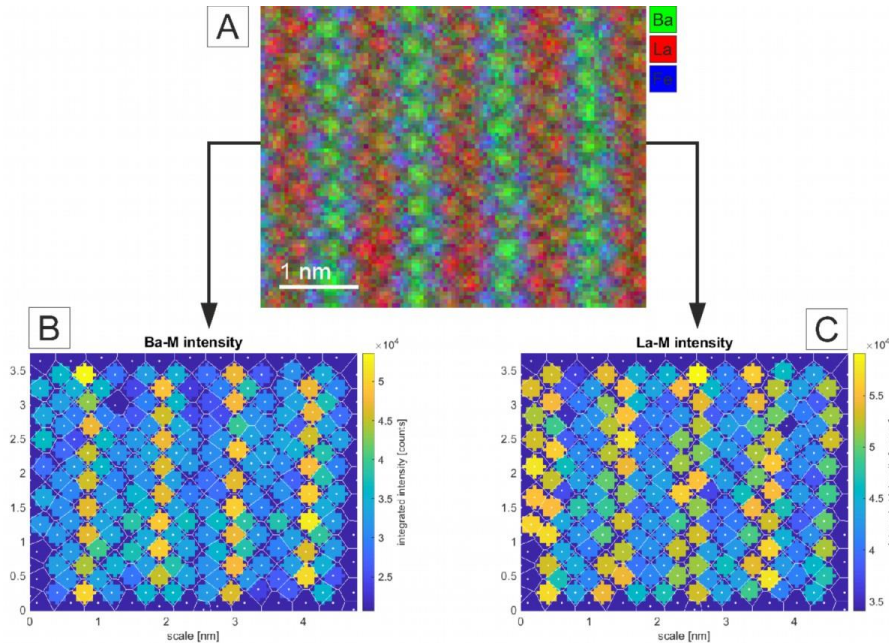


Figure 9: (A) EELS elemental map RGB overlay of Ba (green), La (red) and Fe (blue) of $Ba_{1.1}La_{1.9}Fe_2O_7$ in $[1\ 0\ 0]$ zone axis. (B) and (C) integrated intensities on each atomic columns of Ba (B) and La (C). [6]

2D electron gas (2DEG) can occur at interfaces and exhibit properties absent in the bulk counterpart. The 2DEG occurring at the $GdO_x/SrTiO_3$ interface exhibit an unexpected very large linear magnetoresistance (MR). STEM measurements reveals a mesoscopic structure (formation of GdO_x blisters, self-organized during the growth process). EELS has been performed at atomic resolution and sub-100meV resolution giving the possibility to measure quantitatively electron occupations in these 2D gazes. It reveals an electronic lateral inhomogeneity of ca. 50 nm at the origin of the large linear MR (through a Parish-Littlewood model of magnetotransport in inhomogeneous conductors, Figure 10) [7].

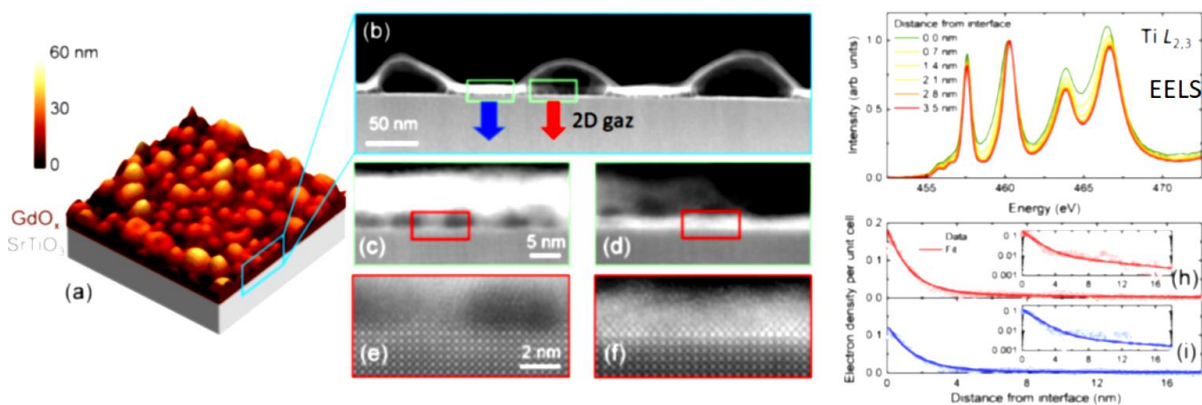


Figure 10: Microscopic investigation of $GdO_x/SrTiO_3$ mesostructures. a) AFM images, b) STEM images and c) EELS spectroscopy. [7]

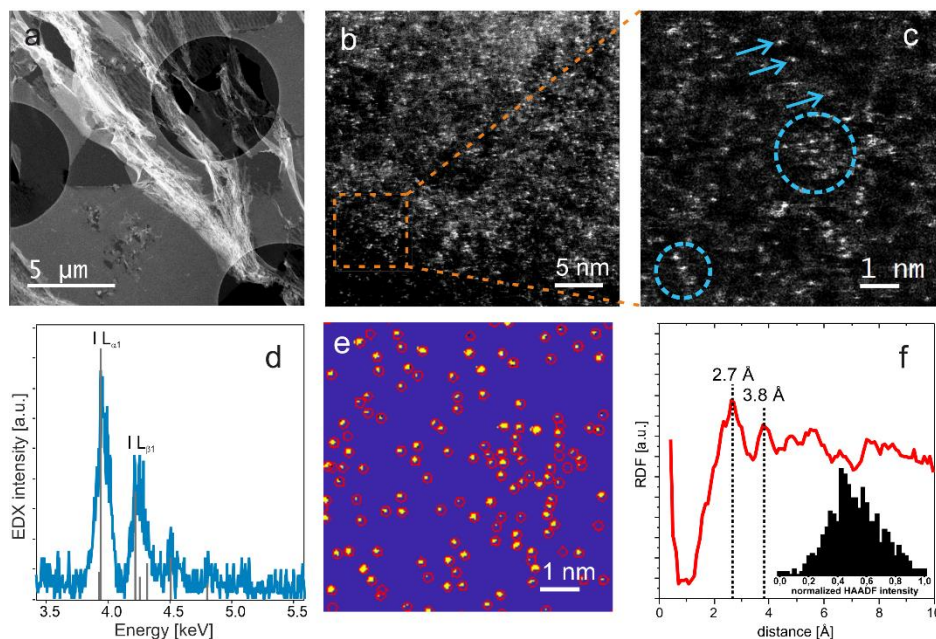


Figure 12: TEM analysis of an I doped carbon electrode: (a) STEM HAADF overview image of the microtome cut suspended over the TEM grid. (b) EDX spectrum demonstrating the presence of iodine. (c) High-resolution STEM HAADF micrograph showing the distribution of iodine atoms in the carbon matrix. (d) magnified region marked in (c). I atoms and clusters are exemplary highlighted by arrows and circles, respectively. (e) result of the automatic segmentation procedure of the region depicted in (d). (f) radial distribution function calculated from obtained atom positions in (c). The histogram in the inset represents a quantitative analysis of the normalized intensities corresponding to detected features. [9]

Task 7.3: Photonic materials (GRA, ZAR, STU, ORS, CHA)

The characterization of photonic materials and the understanding of the manifold phenomena found in nano-optics through TEM and related methods is a highly dynamic branch in this work package, manifested by the number of different systems, physical effects and potential applications - an overview shall be given.

The optical response of 2D semiconductors is usually probed through photoluminescence, reflectivity difference, or extinction experiments. In the first of the following work, we show how similar quantities can be extracted from electron spectroscopies (cathodoluminescence, CL, and electron energy loss spectroscopy, EELS) for these materials. Using these techniques, we observe in an h-BN/WS₂/h-BN heterostructure a local modulation of the trion (X⁻) emission while the neutral exciton, X_A, does not follow the same modulation (Figure 13). Structural and chemical measurements show that these are linked the presence of tens of nanometer wide dielectric patches. Moreover, trion emission also increases in regions, where charge accumulation occurs, close to the carbon film supporting the heterostructures. Finally, we observed that localized exciton emission (L) detection is not correlated to strain variations above 1%, suggesting point defects might be involved in their formations [10].

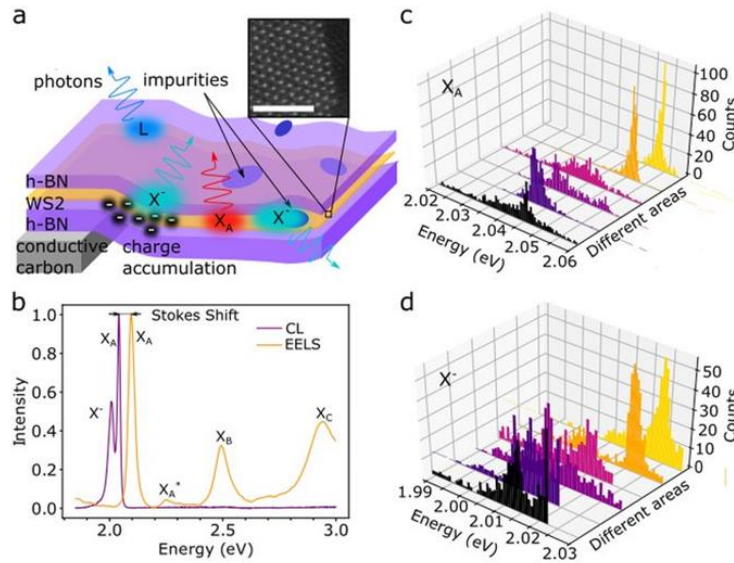


Figure 13: Nanoscale optics of WS_2 monolayers: (a) Sketch of the main results: a WS_2 mono-layer encapsulated by two h-BN flakes shows three emission lines: A excitons (X_A), trions (X^-) and localized emitters (L). (b) Typical electron energy loss spectra (EELS) and cathodoluminescence (CL). (c,d) Correlated histograms of the X_A exciton energy and of the X^- trions energy measured from 6 different areas. [10]

In the second of these works, we report the local study of the optoelectronic properties of $Mo_xW_{(1-x)}S_2$ nanoflakes. For achieving this comprehensive study, we have performed high-resolution scanning TEM (HRTEM) imaging and monochromated electron energy-loss spectroscopy (EELS) measurements. We have then investigated the evolution of the optical band gap and other excitonic features as well as different DOS singularities (Van Hove contributions) of these 2D nanomaterials as a function of the number of layers and alloying degree (content of molybdenum, Figure 14). These studies delve deeper into the optoelectronic properties of atomically thin 2D layers of transition metal dichalcogenide alloys, unveiling potential future applications for this kind of materials [11].

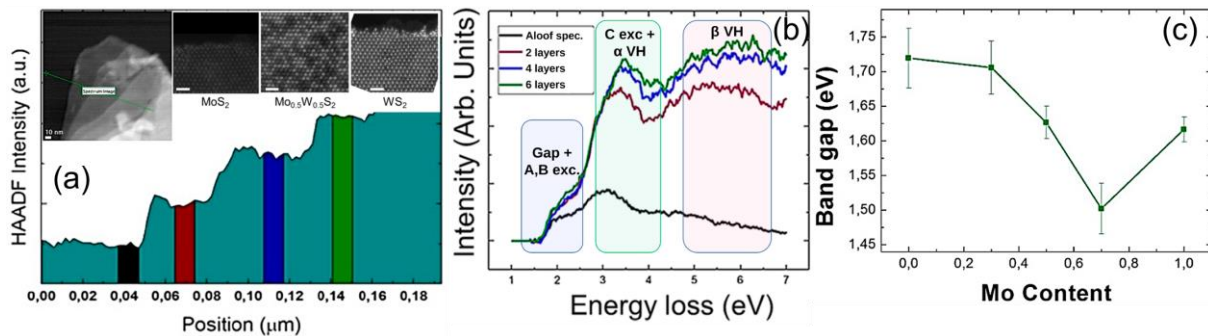


Figure 14: (a) Characterisation of atomically thin $Mo_{0.5}W_{0.5}S_2$ flake, HAADF-STEM micrograph. The location of the STEM-EELS spectrum-line is marked using a green line. HAADF-STEM intensity along the spectrum line. Region in black shows the spectra pertaining to aloof spectroscopy. Highlighted flat windows show areas with the same number of layers, where spectra have been integrated. Insert (Right) HAADF-STEM micrographs of MoS_2 (left), $Mo_{0.5}W_{0.5}S_2$ (center) and WS_2 (right) samples. The difference in contrast between the Mo and S atoms can be seen in the micrograph corresponding to $Mo_{0.5}W_{0.5}S_2$ in the form of brighter and dimmer spots. Scale bar: 1 nm. (b) Integrated spectra from the regions highlighted in Figure 12(a) of a $Mo_{0.5}W_{0.5}S_2$ flake. Same colours are assigned to the integrating window and integrated spectra for clarity. Three different regions of interest are highlighted: The one corresponding to the study of the band gap and the presence of the A and B excitonic features (blue), the one corresponding to the C excitonic feature, overlapped as well with the α van Hove feature (green) and the one corresponding to the β van Hove feature. (c) Band gap as a function of the Mo content for Richardson-Lucy deconvoluted EELS spectrum-line. The error bars represent the statistical deviation among measurements. [11]

The direct-write fabrication of freestanding nanoantennas for plasmonic applications is a challenging task, as demands for overall morphologies, nanoscale features, and material qualities are very high. Within the small pool of capable technologies, three-dimensional (3D) nanoprinting via focused electron beam-induced deposition (FEBID) is a promising candidate due to its design flexibility. However, as FEBID materials notoriously suffer from high carbon contents, the chemical postgrowth transfer into pure metals is indispensably needed, which can severely harm or even destroy FEBID-based 3D nanoarchitectures. Following this challenge, we first dissect FEBID growth characteristics and then combine individual advantages by an advanced patterning approach. The quality of the resulting antennas, in terms of morphology, grain size, chemical composition and plasmonic activity, is assessed by using bright field TEM imaging, STEM-EDX, monochromated STEM-EELS and Raman experiments. By this we demonstrate the direct-write fabrication of high-fidelity shapes with nanoscale features in the sub-10 nm range, which allow a shape-stable chemical transfer into plasmonically active Au nanoantennas. Figure 15 shows the TEM images of the tip region of such a nano-antenna before and after the purification step [12].

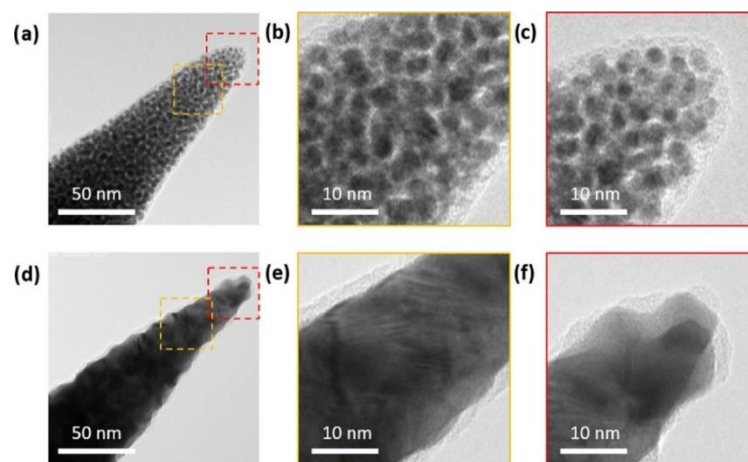


Figure 15: TEM measurements of α -pillars at the tip region before (a–c) and after 300 s (d–f) purification, executed at 30 keV/8.7 nA in 80 Pa H₂O atmospheres at room temperatures. As-deposited AuCX nanopillars (a–c) reveal the typical metal–matrix composition with Au nano-grains (dark), which are embedded in a carbon matrix (bright). After purification, the inner structure dramatically changes into densely packed Au grains with tight interfaces (d–f). While (a) and (d) show overviews, (b, e) and (c, f) are taken from the frames indicated in yellow and red, respectively. [12]

Silver is considered to be the king among plasmonic materials, because it features low inelastic absorption in the visible and infrared (vis-IR) spectral regions compared to other metals. In contrast, copper is commonly regarded as being too lossy for plasmonic applications. We experimentally demonstrate vis-IR plasmons in long copper nanowires (NWs) with quality factors that exceed a value of 60, as determined by spatially resolved, high-resolution electron energy-loss spectroscopy (EELS) measurements (Figure 16). We explain this counterintuitive result by the fact that plasmons in these metal wires have most of their electromagnetic energy outside the metal, and thus, they are less sensitive to inelastic losses in the material. These results support the use of copper as an attractive cheap and abundant material platform for high quality plasmons in elongated nanostructures [13].

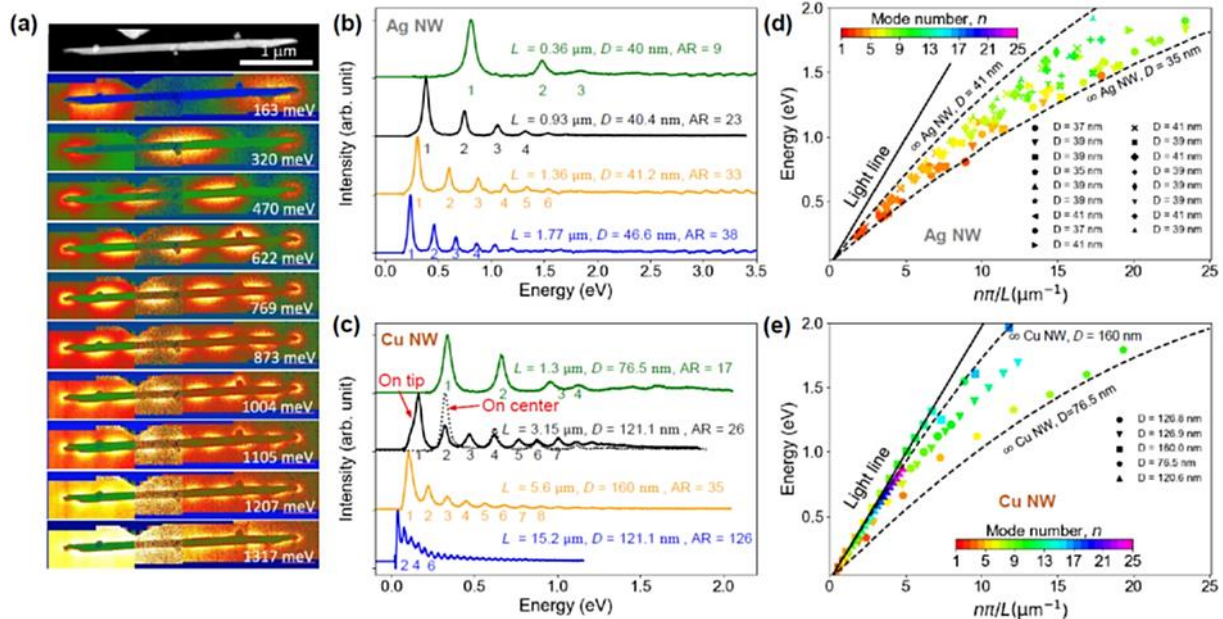


Figure 16: Infrared plasmons in long Ag and Cu NWs. (a) STEM images and the EELS plasmons of (b) Ag and (c) Cu Nanowires. (d, e) dispersion relations obtained from experiment and calculations. [13]

Surface phonon polaritons (SPhPs) are coupled photon-phonon excitations that emerge at the surfaces of nanostructured materials. Although they strongly influence the optical and thermal behavior of nanomaterials, no technique has been able to reveal the complete three-dimensional (3D) vectorial picture of their electromagnetic density of states. Varying SPhP signatures from nanoscale MgO cubes as a function of the beam position, energy loss, and tilt angle, have been observed using a highly monochromated electron beam in a STEM. The SPhPs' response was described in terms of eigenmodes and used to tomographically reconstruct the phononic surface electromagnetic fields of the object. The result of the reconstruction is shown in Figure 17. Such 3D information promises insights in nanoscale physical phenomena and is invaluable to the design and optimization of nanostructures for fascinating new uses [14].

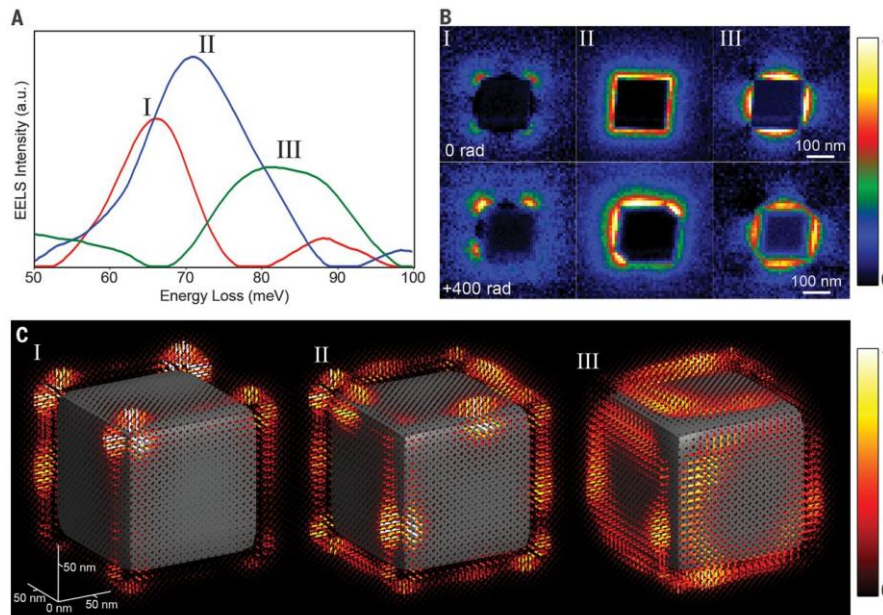


Figure 17: 3D, fully vectorial reconstruction of the phononic electromagnetic local density of state (EMLDOS). (A) NMF components extracted from the experimental data. (B) Reconstructed NMF maps for the three components at two different angles (C) 3D reconstruction of the EMLDOS seen from the top (the substrate, not shown, is at the bottom of the cube). The polarization of the EMLDOS along three orthogonal directions is shown as needles (color and length indicate its intensity). [14]

Task 7.4: Sample preparation (GRA, ZAR, STU, CHA, TOU*, CAT*)

Careful sample preparation is crucial for high-resolution transmission electron microscopy of semiconductor materials and devices. Such samples are mostly prepared using Focused Ion Beam (FIB) milling harnessing Ga ions. Within the scope of a master thesis, we take an alternative approach to explore a combination of different mechanical and ion thinning methods to achieve comparable or even better results compared to traditional FIB preparation. Samples of silicon, silicon germanium, germanium and gallium nitride are prepared both in plan view and in cross-sectional view. The quality of each prepared sample is assessed based on visible defects and artefacts, the sample thickness and the processing time.

Therefore, we use bright-field TEM imaging combined with t/λ maps, which are obtained via EFTEM imaging, providing information about the sample thickness in units of the inelastic electron mean-free path λ . Based on this information the preparation procedures are optimized and documented in detail, with the aim to reproduce them as closely as possible. Figure 18 exemplary shows t/λ maps of GaN samples prepared with two different thinning techniques in comparison. A protocol for the optimized preparation steps will be made available online.

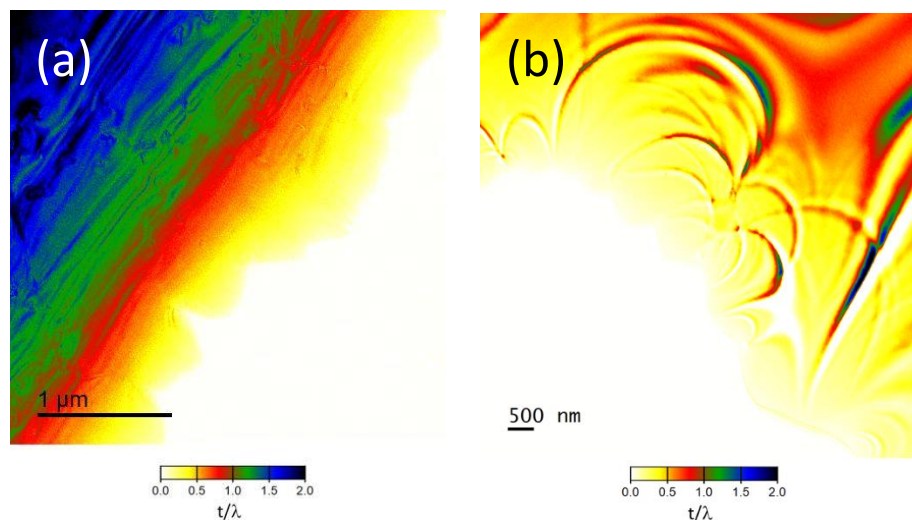


Figure 18: t/λ thickness maps of two GaN samples prepared with an optimized wedge polishing procedure followed by Ar ion milling in (a) and mechanical dimpling followed by ion milling in (b).

Doping elements have a tremendous impact on the properties of functional materials. Therefore, their distribution and characterization are of high importance for manifold applications. The change in physical properties of a doped material can reach from optical characteristics up to modified electrical or magnetic properties. In particular, the properties of photocatalytic oxide materials, such as SrTiO_3 , can be dramatically improved by integrating foreign atoms like Nb, Ta or Rh in trace concentrations. We developed and improved techniques for the preparation using wedge polishing and characterisation of such samples in order to localize single dopant atoms within the crystal by quantitative HAADF imaging supported by quantitative multi-slice simulations. Our results for Ta (0.01 wt.%) doped SrTiO_3 (STO) are shown in Figure 19. Ta preferentially occupies the Ti positions within the perovskite configuration. A sample thickness of less than 5 nm was measured via position-averaged CBED (PACBED). Under such conditions we were able to localize Ta dopants on the TiO column positions of STO in [100] orientation. Furthermore, a drop in intensity within certain Sr columns is detected, which is likely caused by the presence of Sr vacancies within such columns. [In preparation]

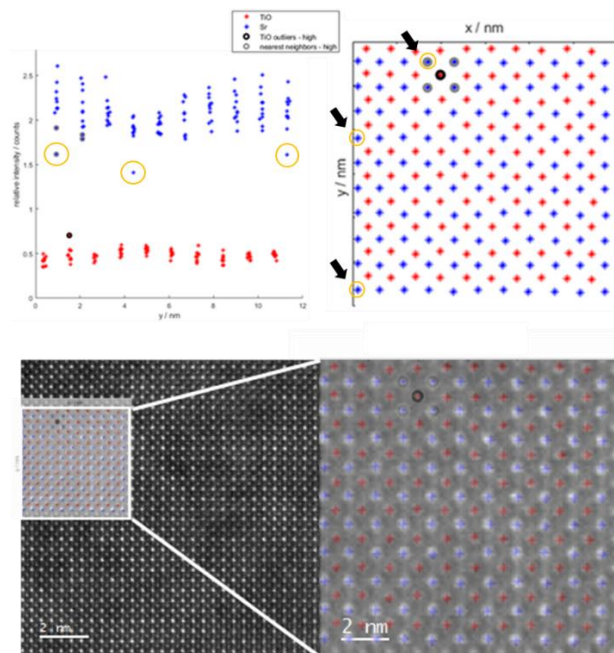


Figure 19: Analysis of a HAADF image section with side view (top left) and top view (top right) as well as overlay results. Ta dopant position marked with black circle and with nearest Sr neighbours in grey, Sr vacancies in orange.

Summary

In summary, all the works presented in this report, which have been developed in the framework of this work package, have illustrated the possibilities that different (scanning) transmission electron microscopy techniques can offer for studying a large variety of ICT materials. These studies have provided rich structural, chemical information as well as they have allowed the study of physical (optical, vibrational, optoelectronic, mechanical) properties of such materials. In the course of this project, further investigations combining some of these techniques with complementary macroscopic techniques as XPS, Raman spectroscopy, optical and infrared spectroscopy ... will continue offering the possibility to study deeper this kind ICT materials, which is critical for their development and further applications.

References (selected papers only)

- [1] Lunjie Zeng, Jonatan Holmér, Rohan Dhall, Christoph Gammer, Andrew M. Minor, Eva Olsson, "Tuning hole mobility of individual p-GaAs nanowires using uniaxial tensile stress – an in situ mechanical and electrical TEM study on III-V nanowires, *Nano Lett.* 21, 3894 (2021).
- [2] Kanne, T., Marnauza, M., Olsteins, D. *et al.* Epitaxial Pb on InAs nanowires for quantum devices. *Nat. Nanotechnol.* **16**, 776–781 (2021).
- [3] Ngabonziza, P., Merkle, R., Wang, Y., van Aken, P. A., Bjørheim, T. S., Maier, J., Mannhart, J., 2D Doping of Proton Conductors: BaZrO₃-Based Heterostructures. *Adv. Energy Mater.* 2021, 11, 2003267.
- [4] Ngabonziza, P., Wang, Y., van Aken, P. A., Maier, J., Mannhart, J., Inelastic Electron Tunneling Spectroscopy at High-Temperatures. *Adv. Mater.* 2021, 33, 2007299.

- [5] Eric Langenberg, Laura Maurel, Guillermo Antorrena, Pedro A. Algarabel, César Magén, José A. Pardo, “Relaxation Mechanisms and Strain-Controlled Oxygen Vacancies in Epitaxial SrMnO₃ Films”, ACS Omega, 6, 13144–13152 (2021).
- [6] Lammer, Judith; Berger, Christian; Löffler, Stefan; Knez, Daniel; Longo, Paolo; Kothleitner, Gerald et al.: A Method for a Column-by-Column EELS Quantification of Barium Lanthanum Ferrate. In Ultramicroscopy under review.
- [7] Mallik et al., “From low-field Sondheimer oscillations to high-field very large and linear magnetoresistance in a SrTiO₃-based two-dimensional electron gas”, accepted in Nanoletters ([arXiv:2108.07612](https://arxiv.org/abs/2108.07612)).
- [8] M. B. Sreedharaa, Simon Hettler, Ifat Kaplan-Ashiri, Katya Rechav, Yishay Feldman, Andrey Enyashin, Lothar Houben, Raul Arenal, Reshef Tenne, “Asymmetric misfit nanotubes: Chemical affinity outwits the entropy at high-temperature solid-state reactions”, Proceedings of National Academy of Sciences, 118, e2109945118 (2021).
- [9] Fitzek, Harald; Sterrer, Martin; Knez, Daniel; Schringer, Horst; Sarapulova, Angelina; Dsoke, Sonia et al. “Tracking the charge transfer effects on the electrified carbon/iodine interface”. In Advanced Science under review.
- [10] Bonnet et al., “Nanoscale modification of WS₂ trion emission by its local electromagnetic environment”, Nano Letters, *in press* (2021) and arXiv:2102.06140 (2021)
- [11] M. Pelaez-Fernandez, Y.-C. Lin, K. Suenaga, R. Arenal, “Optoelectronic Properties of Atomically Thin MoxW(1-x)S₂ Nanoflakes Probed by Spatially-Resolved Monochromated EELS”, Nanomaterials 11, 3218 (2021).
- [12] Kuhness, David; Gruber, Alexander; Winkler, Robert; Sattelkow, Jürgen; Fitzek, Harald; Letofsky-Papst, Ilse et al. (2021): High-Fidelity 3D Nanoprinting of Plasmonic Gold Nanoantennas. In ACS Applied Materials & Interfaces 13 (1), pp. 1178–1191.
- [13] Mkhitarian et al., “Can Copper Nanostructures Sustain High-Quality Plasmons?”. Nano Letters 21, 2444-2452 (2021)
- [14] Li, Xiaoyan; Haberkorn, Georg; Hohenester, Ulrich; Stéphan, Odile; Kothleitner, Gerald; Kociak, Mathieu (2021): Three-dimensional vectorial imaging of surface phonon polaritons. In Science (New York, N.Y.) 371 (6536), pp. 1364–1367. DOI: 10.1126/science.abg0330.
- [15] Magén C., Pablo-Navarro J., De Teresa JM. “Focused-Electron-Beam Engineering of 3D Magnetic Nanowires”, Nanomaterials 11, 402 (2021).